Journal of Nuclear Materials 452 (2014) 311–320

Contents lists available at ScienceDirect

Journal of Nuclear Materials

journal homepage: www.elsevier.com/locate/jnucmat

# Modeling and simulation of hydrogen behavior in Zircaloy-4 fuel cladding

Olivier Courty [a,1], Arthur T. Motta [b,*], Jason D. Hales [c,2]

[a] Pennsylvania State University, 45 Bd Gouvion Saint Cyr, 75017 Paris, France
[b] Department of Mechanical and Nuclear Engineering, 227 Reber Building, Penn State University, University Park, PA 16802, United States
[c] Fuels Modeling & Simulation Department, Idaho National Laboratory, United States

ARTICLE INFO

*Article history:*
Received 22 October 2013
Accepted 4 May 2014
Available online 14 May 2014

ABSTRACT

As a result of corrosion during normal operation in nuclear reactors, hydrogen can enter the zirconium-alloy fuel cladding and precipitate as brittle hydride platelets, which can severely degrade the cladding ductility. Under a heterogeneous temperature distribution, hydrides tend to accumulate in the colder areas, creating local spots of degraded cladding that can favor crack initiation. Therefore, an estimation of the local hydride distribution is necessary to help predict the risk of cladding failure. The hydride distribution is governed by three competing phenomena. Hydrogen in solid solution diffuses under a concentration gradient due to Fick's law and under a temperature gradient due to the Soret effect. Precipitation of the hydride platelets occurs once the hydrogen solubility limit is reached. A model of these phenomena was implemented in the 3D fuel performance code BISON in order to calculate the hydrogen distribution for arbitrary geometries, such as a nuclear fuel rod, and is now available for BISON users. Simulations have been performed on simple geometries to validate the model and its implementation. The simulations predict that before precipitation occurs, hydrogen tends to accumulate in the colder spots due to the Soret effect. Once the solubility limit is reached, hydrogen precipitates and forms a rim close to the outer edge of the cladding. The simulations also predict that the reactor shut down has little effect on already precipitated hydrides but causes the remaining hydrogen to precipitate homogeneously into hydrides.



## 1. Introduction

The core of a Light Water Reactor (LWR) contains fuel assemblies that are cooled by water. The fuel rods in these assemblies are sheathed in the nuclear fuel cladding, made of various zirconium alloys. This fuel cladding serves as a barrier to prevent fission products from escaping into the primary coolant water. The outer wall of the cladding undergoes corrosion when in contact with the cooling water at a temperature range from 280 °C to 340 °C. The corrosion reaction generates hydrogen, a fraction of which is picked up by the cladding.

Once the hydrogen enters the cladding, it can either be dissolved in solid solution in the α-Zr matrix or precipitated as zirconium hydrides. The hydrogen in solid solution corresponds to H atoms occupying interstitial sites in the hcp zirconium structure [1]. At higher concentrations, hydrogen precipitates and forms hydrides (mostly delta hydrides) [2]. These hydrides are inhomogeneously distributed within the cladding tube, and in high enough concentration they can severely degrade cladding ductility [3].

During operation, temperature gradients exist in the cladding, in the axial, radial and azimuthal directions, so that hydrogen distribution, in response to those gradients, can become inhomogeneous, and local high hydride concentration regions can occur. Fig. 1.1 is a schematic of these different features.

A radial gradient in the hydride distribution is normally observed in fuel rods exposed to the LWR environment. After long exposures (>4 years), a high hydride concentration region is observed, constituting a hydride "rim". A hydride rim is observed close to the outer edge of the cladding, where the temperature is the lowest [4]. A study of Bossis et al. [5] shows that at high burnup, the average hydrogen concentration in the rim is on the order of 1300 wt. ppm, while the cladding average concentration is 430 wt. ppm.

Because of the heat production in the fuel, the coolant temperature gradually increases with height along the axial direction. Just after the spacer grid mixing vanes, local decreases in temperature

* Corresponding author. Tel.: +1 814 865 0036; fax: +1 814 865 1280.
*E-mail addresses:* o.courty@gmail.com (O. Courty), atm2@psu.edu (A.T. Motta), jason.hales@inl.gov (J.D. Hales).
[1] Tel.: +33 661568180; fax: +33 1 70 75 63 03.
[2] Tel.: +1 (208) 526 2293.

http://dx.doi.org/10.1016/j.jnucmat.2014.05.013
0022-3115/

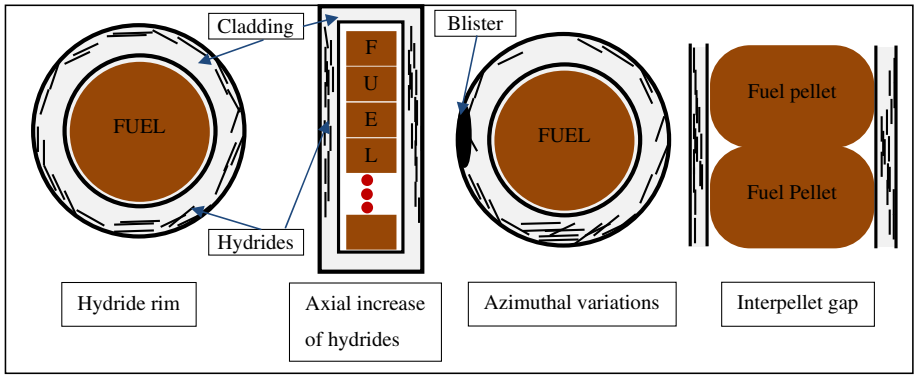


**Fig. 1.1.** Schematic of typical hydride distribution: Hydride rim, axial increase, azimuthal variations and interpellet gap.

are also seen, caused by improved heat transfer associated with better mixing of the coolant flow. The oxide growth follows the same profile as the temperature, increasing generally and decreasing locally at the spacer grids locations [6]. As a consequence, the amount of hydrogen picked up increases with height.

Another common observation regarding the temperature dependence of hydrogen distribution is the enhancement of the concentration of hydride at the inter-pellet gaps. The lower heat flux causes a slight decrease in temperature which can cause hydride to concentrate. The work by Garde and co-workers [7] shows a high concentration of hydrides close to the inter-pellet gap, compared to the mid-pellet cladding, as shown schematically in Fig. 1.1.

In the azimuthal direction, a hydrogen temperature distribution can also occur because of the heterogeneity of the core geometry. Guide tubes, corners and sides of the assemblies can create colder temperature regions that can increase local hydride concentration. This is the least well-known hydride heterogeneity, but evidence for this has been given by Billone and co-workers who observed for a cladding with 600 wt. ppm average hydrogen concentration, a range around the azimuth from 400 wt. ppm to 800 wt. ppm [4]. Hydride blisters can also form when oxide spallation occurs [8].

Because the overall cladding ductility is often effectively limited by the highest hydrogen concentration region, it should be clear from the preceding discussion that the cladding ductility is intimately dependent on the local hydride concentration, and thus an accurate representation of the detailed temperature distribution and a reliable model of hydrogen transport and precipitation is needed to evaluate the overall ductility of the full range of fuel rods found in PWR cores. The aim of this study is to present a model of hydrogen behavior and describe its implementation into the BISON fuel performance code, which allows for the simultaneous solution of hydrogen and temperature distributions.

## 2. Modeling hydrogen redistribution

The hydrogen picked up by the cladding has its distribution altered by three main phenomena: (i) the hydrogen in solid solution diffuses under a concentration gradient due to Fick's law, (ii) the hydrogen in solid solution diffuses under a temperature gradient due to the Soret effect; (iii) finally hydrogen in solid solution can precipitate into hydrides once the concentration reaches the terminal solid solubility ($TSS_p$) for precipitation. The modeling of these phenomena is shown in the following section. Although the hydrogen distribution is also affected by stress gradients [9,10] and by microstructural features such as grain boundaries and intermetallic precipitates, the current model does not yet consider these effects.

### 2.1. Transport of hydrogen

#### 2.1.1. Diffusion under a concentration gradient: Fick's law

A concentration gradient in the hydrogen distribution generates a flux according to Fick's law [11]. This concerns only the hydrogen in solid solution, as the hydrogen in the hydride phase is not mobile.

$$J_{\text{Fick}} = -D \cdot \nabla C_{ss} \tag{1}$$

where $J_{\text{Fick}}$ is the diffusion flux due to concentration gradient, $C_{ss}$ the concentration of hydrogen in solid solution, T the temperature in K and D the hydrogen diffusion coefficient in Zircaloy, which is written in Arrhenius form as:

$$D = A_D \cdot \exp\left(-\frac{Q_D}{R \cdot T[\text{K}]}\right) \tag{2}$$

where $Q_D$ is the activation energy for diffusion and $A_D$ is a constant.

The coefficients have been measured by Kearns [11], for a temperature expressed in Kelvin as $A_D = 7.90 \times 10^{-7}$ m$^2$/s and $Q_D = 4.49 \times 10^4$ J/mol.

#### 2.1.2. Diffusion under temperature gradient: Soret effect

As observed by Sawatzky [12] and confirmed in several studies [13–21], hydrogen diffusion is also driven by a temperature gradient. According to the linear thermodynamic model [22], there is a coupling between the thermal gradient and chemical diffusion. This phenomenon is called the Soret effect. The diffusion flux due to the temperature gradient is given by [12]:

$$J_{\text{Soret}} = -\frac{DC_{ss}Q^*}{RT^2}\nabla T \tag{3}$$

where $J_{\text{Soret}}$ is the diffusion flux due to the Soret effect and $Q^*$ is the heat of transport.

Different values of $Q^*$ have been measured in the literature [13,19,21,23]. This study assumes a $Q^*$ value equal to 25.1 kJ/mol, based on Kammenzind's measurements performed in Zircaloy-4 [21]. The combined diffusion flux under concentration gradient and temperature gradient is given by:

$$J_{\text{diffusion}} = -D\nabla C_{ss} - \frac{DC_{ss}Q^*}{RT^2}\nabla T \tag{4}$$

### 2.2. Hydride precipitation

#### 2.2.1. Terminal solid solubility

When the hydrogen content reaches the terminal solid solubility (TSS) in the α-zirconium matrix, hydrides are formed. The hydrides observed in fuel cladding are most often FCC delta hydrides $ZrH_{1.66}$ [2]. Kearns' study on the TSS using the diffusion

couple method has been widely used as the reference for TSS determination [24].

A hysteresis phenomenon has been observed in several studies between the TSS for dissolution ($TSS_d$) and the TSS for precipitation ($TSS_p$). This temperature hysteresis is a result of the additional energy associated with the volume expansion that accompanies hydride precipitation. According to McMinn [25], the $TSS_d$ and the $TSS_p$ for unirradiated Zircaloy can be approximated by the following equations:

$$\begin{cases} TSS_d[\text{wt. ppm}] = 106446.7 \cdot \exp\left(-\dfrac{4328.67}{T[\text{K}]}\right) \\ TSS_p[\text{wt. ppm}] = 138746.0 \cdot \exp\left(-\dfrac{4145.72}{T[\text{K}]}\right) \end{cases} \quad (5)$$

Eq. (5) have been used in the current study to calculate the $TSS_p$ and the $TSS_d$. Other parameters, such as irradiation, stress and alloying elements, may change the $TSS_p$ and the $TSS_d$, but they have not been considered in this work. We note that other solubility limit equations [21,24] have a greater range of applicability, as this correlation was developed for $H$ levels <80 wt. ppm. Nevertheless, these equations were chosen as the reference for precipitation.

### 2.2.2. Precipitation kinetics

The limited solubility and the kinetics of precipitation are a critical aspect of hydrogen redistribution in the cladding. While the $TSS_p$ and $TSS_d$ describe the hysteresis between the precipitation and dissolution solvus, the kinetics provide information regarding the transient behavior between a non-equilibrated initial condition and the final steady state equilibrium. The detailed kinetics of hydride precipitation is a significant factor in the development of the hydride rim feature and of other specific hydrogen distributions that can occur in nuclear fuel cladding.

In the case of reactor operation, the initial concentration of hydrogen starts at about 5–10 wt. ppm. The cladding is subjected to a temperature gradient of about 60 °C/mm over the cladding. The hydrogen flux is coming from the coolant interface as a result of the corrosion pickup. As noted by Shewmon [26], it is not possible to predict the redistribution solely from the diffusion laws and the Terminal Solid Solubility. Indeed, as long as the hydrogen concentration does not reach the $TSS_p$, the equilibrium is established in a quasi-steady-state manner, following Eq. (6), as calculated by Sawatzky [13].

$$C_{ss} = K_{\text{int}} \cdot \exp\left(\frac{Q^*}{RT}\right) \quad (6)$$

where $Q^*$ is the heat of transport of hydrogen in Zircaloy and $K_{\text{int}}$ is an integration constant that depends on the initial conditions and that can be obtained by applying the conservation of mass of hydrogen. The highest concentration of hydrogen will occur in the colder area, which is the coolant/cladding interface.

Moreover, the $TSS_p$ decreases when the temperature decreases. Therefore the area with the lowest temperature also shows the lowest $TSS_p$. Thus, the hydrogen concentration first reaches the $TSS_p$ at the cladding/coolant interface. If instantaneous precipitation is assumed, there is no reason for the hydrogen to diffuse into the cladding, as it precipitates instantaneously upon entry into the cladding. This would however lead to the formation of a solid hydride rim, which does not correspond to experimental observation. Therefore, the role of precipitation kinetics needs to be examined, to rationalize why hydrogen diffuses into the cladding. If the hydrogen does not precipitate instantaneously, it can remain supersaturated in the solid state. In that case, the previous diffusion equilibrium is modified and hydrogen diffuses toward the inner cladding. As a result, some hydrogen will precipitate further into the cladding, as shown schematically in Fig. 2.1.

The precipitation kinetics used in this study follows the model developed by Marino [27,28], who proposed that the precipitation rate is proportional to the difference between supersaturated hydrogen in solid solution concentration $C_{ss}$ and the equilibrium value (given by the $TSS_p$):

$$\frac{dC_{ss}}{dt} = -\alpha^2(C_{ss} - TSS_p) \quad (7)$$

The kinetics parameter $\alpha^2$ has been measured by Kammenzind, who proposed an Arrhenius law to describe its dependence on temperature [21]. The equation found for $\alpha^2$ is:

$$\alpha = A_\alpha \cdot \exp\left(-\frac{Q_\alpha}{RT}\right) \quad (8)$$

with $A_\alpha \approx 62.3\ s^{-1/2}$ and $Q_\alpha \approx 4.12 \times 10^4$ J/mol

### 2.3. Balance equation for hydrogen in solid solution and precipitated hydrogen

From the precipitation, dissolution and diffusion models explained in the previous sections, a balance equation for hydrogen in solid solution and hydride concentration can be derived. As described by Eq. (9), the variation of hydrogen in solid solution per unit time is given by the sum of the net flux, the hydrogen created by the dissolution of hydride minus the hydrogen transformed into hydride due to precipitation.

$$\left\{ \begin{array}{l} \dfrac{dC_{ss}}{dt} = -\nabla \cdot J - R_{\text{precipitation}} + R_{\text{dissolution}} \\ \dfrac{dC_{pp}}{dt} = R_{\text{precipitation}} - R_{\text{dissolution}} \end{array} \right\} \quad (9)$$

where $C_{SS}$ is the concentration of hydrogen in solid solution, $C_{pp}$ the concentration of hydrogen in hydride precipitates, $J$ is the diffusion flux, $R_{\text{precipitation}}$ and $R_{\text{dissolution}}$ are the rates of precipitation and dissolution respectively.

Hydride precipitation occurs when the concentration of hydrogen in solid solution surpasses the $TSS_p$. Hydride dissolution occurs when the concentration of hydrogen in solid solution becomes lower than the $TSS_d$. Four different cases have to be taken into account for the writing of the balance equations.

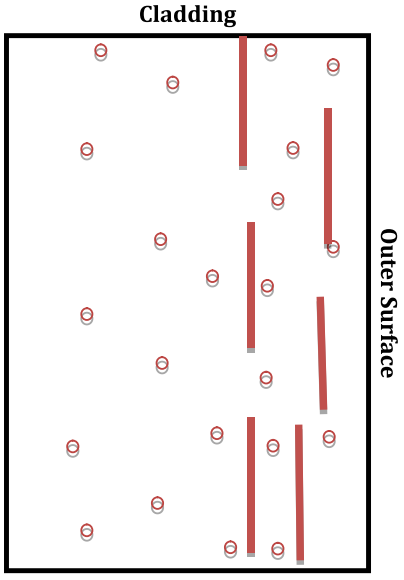


**Fig. 2.1.** Schematic of the hydrogen and hydride distribution in the cladding.

*2.3.1. Case 1: precipitation*

In the first case, the concentration of hydrogen in solid solution in a unit volume is greater than the $TSS_p$. In this case, the variation of hydrogen in solid solution per unit of time is equal to the net flux minus the amount of hydrogen that is transformed into hydrides.

$$If \quad C_{ss} > TSS_p, \left\{ \begin{array}{c} \frac{dC_{ss}}{dt} = -\nabla \cdot J - \alpha^2 (C_{ss} - TSS_p) \\ \frac{dC_{pp}}{dt} = \alpha^2 (C_{ss} - TSS_p) \end{array} \right\} \tag{10}$$

where again $C_{ss}$ is the amount of hydrogen in solid solution, expressed in wt. ppm. $C_{pp}$ is the amount of hydrogen precipitated in hydrides, expressed in wt. ppm.

*2.3.2. Case 2: hysteresis*

In the second case, the concentration in solid solution lies between the $TSS_p$ and the $TSS_d$. This is the "hysteresis" area, where neither dissolution nor precipitation occurs. Only the hydrogen in solid solution responds to temperature and concentration gradients.

$$\text{If} \quad TSS_p \geqslant C_{ss} > TSS_d, \left\{ \begin{array}{c} \frac{dC_{ss}}{dt} = -\nabla \cdot J \\ \frac{dC_{pp}}{dt} = 0 \end{array} \right\} \tag{11}$$

*2.3.3. Case 3: dissolution*

In the third case, the concentration in solid solution is below the $TSS_d$, and hydrides are present ($C_{pp} > 0$). The hydrogen in the precipitated hydrides ($C_{pp}$) is dissolving so that the $C_{ss}$ matches the $TSS_d$ value.

$$\text{If} \quad TSS_d \leqslant C_{ss} \quad \text{and} \quad C_{pp} > 0, \left\{ \begin{array}{c} \frac{dC_{ss}}{dt} = -\nabla \cdot J + \beta^2 (TSS_d - C_{ss}) \\ \frac{dC_{pp}}{dt} = -\beta^2 (TSS_d - C_{ss}) \end{array} \right\} \tag{12}$$

where $\beta$ is the kinetics parameter for dissolution. It is usually assumed that dissolution kinetics is very fast compared to precipitation kinetics, so that $\beta^2 \gg \alpha^2$ and $\beta^2 \gg \frac{l^2}{D}$, with $l$ the characteristic length of the geometry.

*2.3.4. Case 4: diffusion only*

In the fourth and last case, the concentration in solid solution is below the $TSS_d$, but no hydrides are present. In that case, the only change to the hydrogen concentration comes from the net diffusion flux.

$$\text{If} \quad TSS_d \geqslant C_{ss} \quad and \quad C_{pp} = 0, \left\{ \begin{array}{c} \frac{dC_{ss}}{dt} = -\nabla \cdot J \\ \frac{dC_{pp}}{dt} = 0 \end{array} \right\} \tag{13}$$

There are physical limits to the amount of hydrides per unit of volume. A first limit is that there cannot be more hydrogen in a given volume than is contained in a stoichiometric hydride, that is, the material is a solid hydride. This amount is given by Eq. (14)

$$C_{pmax} = 1.66 \cdot \frac{M(H)}{M(Zr)} \cdot 10^6 \approx 18,200 \text{ wt.ppm} \tag{14}$$

However, it has been experimentally observed that the maximum amount of hydrogen in the rim falls between 1000 wt. ppm and 2000 wt. ppm [4,5]. Although solid hydrides are observed when blisters form or when hydrogen is charged electrolytically, the hydride rim concentrations observed are normally much lower than the value in Eq. (14) (1000–2000 wt. ppm). There are several possible physical reasons why the hydrogen concentration of the rim is smaller than the theoretical limit. The equilibrium between hydrogen in solid solution and hydrides may be affected by the hydrides that have already precipitated. The precipitation kinetics may be changed by the increase of hydride nuclei, or by a competition between different hydrides. The hydrogen levels in the rim in samples oxidzied in the reactor vary depending on alloy, burnup, etc. The implementation of the model allows the user to choose the maximum value for $C_{pp}$. In the simulations presented in this paper, the maximum was arbitrarily set to 1000 wt. ppm. Once the limit is reached at a given location, no further precipitation can happen at this location. It is clear that this is an artificial limitation, serving here to account for physical phenomena that are not accounted for in the model, such as sympathetic nucleation, and the influence of the asymmetric hydrogen distribution on trapping of hydrogen atoms.

The constants for the hydrogen in Zircaloy-4 model have been taken from the literature and are summarized in Table 2.1.

*2.4. Boundary condition: flux entering the cladding from the coolant/cladding interface*

The hydrogen flux entering the cladding is proportional to the oxidation rate, and its value is needed to obtain a quantitative result. The purpose of the current section is to evaluate this flux from the oxide kinetics equations. The oxidation kinetics have been formulated using semi-empirical models, as detailed in the Waterside Corrosion report, produced by the International Atomic Energy Agency (IAEA) [29]. These models separate two different kinetic behaviors. At first, oxidation weight gain kinetics is governed by a cubic rate law:

$$w^3 = k_c \cdot t, \text{ with } k_c = A_{kc} \cdot \exp\left(-\frac{Q_{kc}}{RT}\right) \tag{15}$$

with: $w$ the weight gain (mg/dm$^2$), $A_{kc}$ the pre-transition frequency factor (in (mg/dm$^2$)$^3$/d), $Q_{kc}$ the pre-transition activation energy for oxide growth during cubic kinetics (J/mol), $R$ the gas constant, $T$ the temperature (K).

Assuming that all oxygen weight gain is used to produce $ZrO_2$ and that no $ZrO_2$ oxide is lost by spallation or dissolution, the oxide layer thickness is proportional to the weight gain [30]:

$$\delta(\mu m) = \frac{w\left(\frac{mg}{dm^2}\right)}{14.7} = \frac{(k_c \cdot t)^{\frac{1}{3}}}{14.7} = K_c^{\frac{1}{3}} \cdot t^{\frac{1}{3}} \tag{16}$$

$K_c$ is the cubic constant for the oxide layer growth, and $k_c$ is the cubic constant for the weight gain evolution.

When the oxide thickness follows a cubic law, the oxidation rate gradually decreases, until at a given oxide thickness ($\delta \approx 1.8 - 2$ μm for Zircaloy-4), a kinetic transition is observed. At this point, often referred to as the oxide transition, the oxidation kinetics return to the initial value seen at the start of the corrosion of the bare metal [31]. Henceforth, the oxidation kinetics can be approximated with a linear rate law:

$$w = k_l \cdot (t - t^*) + w^*, k_l = A_{kl} \cdot \exp\left(-\frac{Q_{kl}}{RT}\right) \tag{17}$$

with: $w$ the weight gain (mg/dm$^2$), $k_l$ the linear rate constant (μm/day), $t^*$ the transition time (days), $w^*$ the weight gain at the transition (mg/dm$^2$), $A_{kl}$ the post-transition frequency factor (in (mg/dm$^2$)/d).

In terms of oxide thickness, Eq. (17) is rewritten as:

$$\delta = \delta^* + K_L \cdot (t - t^*) \tag{18}$$

The kinetics constants in Eqs. 17–20 have been taken from previous work. According to [29], the values given in Table 2.2 have been considered in previous work and fuel performance codes.

**Table 2.1**
Hydrogen model constants in Zircaloy-4.

| Phenomenon | Parameter | Value | Unit | Source | Comments |
|---|---|---|---|---|---|
| Fick's law | $A_{Dff}$ | $7.90 \times 10^{-7}$ | $m^2/s$ | [11] | Longitudinal diffusion |
| | $Q_{Diff}$ | $4.49 \times 10^4$ | J/mol | [11] | Longitudinal diffusion |
| Soret effect | $Q^*$ | $2.51 \times 10^4$ | J/mol | [21] | Average value |
| Precipitation | $A_P$ | $1.39 \times 10^5$ | wt. ppm | [25] | Unirradiated |
| | $Q_P$ | $3.45 \times 10^4$ | J/mol | [25] | Unirradiated |
| Dissolution | $A_D$ | $1.06 \times 10^5$ | wt. ppm | [25] | Unirradiated |
| | $Q_D$ | $3.60 \times 10^4$ | J/mol | [25] | Unirradiated |
| Precipitation kinetics | $A_\alpha$ | $6.23 \times 10^1$ | $s^{-1/2}$ | [21] | |
| | $Q_\alpha$ | $4.12 \times 10^4$ | J/mol | [21] | |

**Table 2.2**
Zircaloy-4 empirical oxidation kinetics parameters.

| Source/model | Pre transition frequency factor $A_{Kc}$ (cubic) $(14.7)^{-3}$ μm³ · d⁻¹ | Pre transition activation energy (Q/R) K | Post transition frequency factor $A_{Kl}$ (linear) $(14.7)^{-1}$ μm³ · d⁻¹ | Post transition activation energy (Q/R) K | Transition oxide thickness $\delta^*$ (μm) or time $t^*$ (days) = $A \exp(-B)$ | |
|---|---|---|---|---|---|---|
| | | | | | A | B |
| | | | | | μm³ · d⁻¹ | K |
| MATPRO [32] | $4.976 \times 10^9$ | 15,660 | $8.288 \times 10^7$ | 14,080 | 7.749 | 790/T |
| EPRI KWU/C-E | $1.78 \times 10^{10}$ | 16,250 | $8.04 \times 10^7$ | 13,766 | $2.14 \times 10^7$ | −5417/T − 0.0117T |
| COCHISE (CEA) | $11.4 \times 10^{10}$ | 17,171 | $4.0 \times 10^{11}$ | 18,391 | $8.857 \times 10^{10}$ | 921/T − 0.035T |

According to the oxidation reaction shown in Eq. (19), there are 4 atoms of hydrogen for each molecule of Zr oxide.

$$Zr + 2H_2O \rightarrow ZrO_2 + 2H_2 \tag{19}$$

A fraction (called the hydrogen pickup fraction) of the hydrogen atoms produced in the oxidation reaction are transported to the oxide-metal interface and are absorbed into the cladding. The absorbed hydrogen is redistributed in the material in response to thermodynamic driving forces, as detailed above. For Zircaloy-4, 10–20% of the hydrogen liberated from corrosion is typically absorbed into the cladding, as has been studied by several authors [33,34] and can vary during corrosion, with axial location and with burnup. A typical value of $f_H = 15\%$ is used here as an average pick-up. The hydrogen flux that enters the cladding at the coolant interface is now calculated. The number of moles of Zr oxide molecules in the oxide layer, per unit surface area, is given by:

$$n_{ZrO_2} = \delta \cdot \frac{\rho(ZrO_2)}{M(ZrO_2)} \tag{20}$$

where $\delta$ is the oxide thickness, $\rho(ZrO_2)$ the oxide density and $M(ZrO_2)$ the oxide molar mass.

The mass of hydrogen picked up by the cladding is then given by:

$$m_H = 4f_H \cdot \delta \cdot \frac{\rho(ZrO_2)}{M(ZrO_2)} \cdot M_H \tag{21}$$

where $M_H$ is the hydrogen molar mass. It is common to use wt. ppm for the concentration of hydrogen. The mass of zirconium (per unit of surface) in the cladding is given by Eq. (22):

$$m_{Zr} = \rho(Zr) \cdot (th_{Zr} - \delta) \tag{22}$$

where $\rho(Zr)$ is the density of pure zirconium and $th_{Zr}$ is the cladding thickness. The thickness corresponds to the initial thickness of the cladding, about 600 μm. For corrosion occurring on the outer cladding surface, the average concentration of hydrogen in the cladding in wt. ppm is given by.

$$C_H(\text{wt. ppm}) = \frac{4f}{1.56} \frac{\delta}{(th_{Zr} - \delta)} \cdot \frac{M_H}{M_{Zr}} \tag{23}$$

From Eqs. (16) and (18), the rate at which the oxide layer thickness increases is:

$$\frac{d(\delta)}{dt} = (K_c)^{\frac{1}{3}} \cdot \frac{1}{3} t^{-\left(\frac{2}{3}\right)} \tag{24}$$

for the cubic regime, and

$$\frac{d(\delta)}{dt} = K_L \tag{25}$$

for the linear regime.

The rate of the increase of hydrogen in the cladding is given by:

$$\frac{dC_H}{dt} = \frac{4f_H}{1.56} \cdot \frac{M_H}{M_{Zr}} \cdot \left(\frac{th_{Zr}}{(th_{Zr} - \delta)^2}\right) \cdot \frac{d\delta}{dt} \tag{26}$$

Conservation of mass implies that:

$$\frac{dC_H}{dt} \cdot V = J \cdot S \tag{27}$$

where $V$ is the volume of cladding considered and $J$ is the flux of hydrogen coming into this volume through the cross-section $S$. The cross-section $S$ multiplied by the cladding thickness is equal to the volume $V$. Therefore:

$$J = th_{Zr} \cdot \frac{4f_H}{1.56} \cdot \frac{M_H}{M_{Zr}} \cdot \left(\frac{th_{Zr}}{(th_{Zr} - \delta)^2}\right) \cdot \frac{d\delta}{dt}$$
$$J = \frac{4f_H}{1.56} \cdot \frac{M_H}{M_{Zr}} \cdot \left(\frac{th_{Zr}^2}{(th_{Zr} - \delta)^2}\right) \cdot \frac{d\delta}{dt} \quad (\text{wt. ppm/cm}^2/\text{s}) \tag{28}$$

To a first approximation, the thickness factor (in parenthesis in Eq. (28)) can be neglected. After 4 years, the oxide thickness is about 30 μm according to the MATPRO model, and the thickness factor is about 1.1. With this approximation the equation becomes:

$$J = \frac{4f_H}{1.56} \cdot \frac{M_H}{M_{Zr}} \cdot \frac{d\delta}{dt} \quad (\text{wt.ppm/cm}^2/\text{s}) \tag{29}$$

Eq. (29) provides an estimation of the hydrogen flux entering the cladding as a result of waterside corrosion for use in our simulations.

## 3. Implementation of the hydrogen model into BISON

BISON is a nuclear fuel performance code designed to perform efficient fully-coupled calculations for steady and transient analysis on both desktop computers and in massively parallel environments. It employs physics-based preconditioned Jacobian-free Newton–Krylov solution methods and is developed using modern software engineering principles to form a robust, extensible software architecture to ultimately provide a design and analysis capability for a wide range of nuclear phenomena [35]. The hydrogen model presented in the previous section has been implemented into BISON. The solution for temperature and hydrogen distributions can be simultaneously computed through the fully-coupled solution strategy in BISON.

### 3.1. Implementation of the hydrogen in solid solution balance equations

In the BISON solution approach, the model equations must be transformed into their weak form. The following derivation is partially inspired from the work of Newman et al. on the treatment of oxygen diffusion [36]. The weak form corresponds to the scalar product (in the function space) of the equation and a test function:

$$\text{Weak Form}\,(f) = (f,\psi) = \int_\Omega f(x,y,z)\cdot\psi_i(x,y,z)d\Omega \tag{30}$$

The function scalar product is represented by $(f, \psi)$, where $f$ is a space and time dependent function and $\psi_i$ is a test function over the domain $\Omega$. In the case of the second derivative in $f$, the weak form allows integration by parts, which eliminates the second order derivative. For instance (applying the divergence theorem for the second term):

$$\text{Weak Form}(\nabla^2 T) = \int_\Omega \nabla^2 T(x,y,z)\cdot\psi_i(x,y,z)d\Omega \tag{31}$$

In Case 1 (precipitation), the balance equation governing the hydrogen in solid solution is:

$$\frac{dC_{ss}}{dt} + \nabla\cdot J + \alpha^2(C_{ss} - \mathrm{TSS}_p) = 0 \tag{32}$$

The weak form is obtained by multiplying Eq. (32) by a test function $\psi_i$ and integrating over $\Omega$:

$$\int_\Omega \frac{dC_{ss}}{dt}\cdot\psi_i\cdot d\Omega + \int_\Omega \nabla.\left(-D\nabla C_{ss} - \frac{DC_{ss}Q^*}{RT^2}\nabla T\right)\cdot\psi_i\cdot d\Omega + \int_\Omega \alpha^2(C_{ss} - \mathrm{TSS}_p)\cdot\psi_i\cdot d\Omega = 0 \tag{33}$$

The second term is then integrated by parts, so that Eq. (33) becomes:

$$\int_\Omega \frac{dC_{ss}}{dt}\cdot\psi_i\cdot d\Omega - \int_\Omega \left(-D\nabla C_{ss} - \frac{DC_{ss}Q^*}{RT^2}\nabla T\right)\cdot\nabla\psi_i\cdot d\Omega + \int_S \left(-D\nabla C_{ss} - \frac{DC_{ss}Q^*}{RT^2}\nabla T\cdot\psi_i\right)\cdot dS + \int_\Omega \alpha^2(C_{ss} - \mathrm{TSS}_p)\psi_i\cdot d\Omega = 0 \tag{34}$$

The third term corresponds to a boundary condition. It is the weak form of the product of the hydrogen flux multiplied by the surface unit vector. This boundary condition is usually called the natural boundary condition or the Neumann boundary condition. Using (,) notation for volume integrals and the < , > notation for the boundary conditions, Eq. (34) becomes:

$$\left(\frac{dC_{ss}}{dt},\psi_i\right) + \left(D\nabla C_{ss} + \frac{DC_{ss}Q^*}{RT^2}\nabla T,\nabla\psi_i\right) + \left\langle -D\nabla C_{ss} - \frac{DC_{ss}Q^*}{RT^2}\nabla T,\psi_i\right\rangle + (\alpha^2(C_{ss} - \mathrm{TSS}_p),\psi_i) = 0 \tag{35}$$

The weak form is obtained in a similar fashion in the case of diffusion. The weak form of Eq. (11) is:

$$\left(\frac{dC_{ss}}{dt},\psi_i\right) + \left(D\nabla C_{ss} + \frac{DC_{ss}Q^*}{RT^2}\nabla T,\nabla\psi_i\right) + \left\langle -D\nabla C_{ss} - \frac{DC_{ss}Q^*}{RT^2}\nabla T,\psi_i\right\rangle + (-\beta^2(\mathrm{TSS}_d - C_{ss}),\psi_i) = 0 \tag{36}$$

In the absence of precipitation and dissolution (Cases 3 and 4), the weak form of the balance equation is:

$$\left(\frac{dC_{ss}}{dt},\psi_i\right) + \left(D\nabla C_{ss} + \frac{DC_{ss}Q^*}{RT^2}\nabla T,\nabla\psi_i\right) + \left\langle -D\nabla C_{ss} - \frac{DC_{ss}Q^*}{RT^2}\nabla T,\psi_i\right\rangle = 0 \tag{37}$$

In order to compute the solution of the equations (through iteration), BISON uses a mathematical tool called the Jacobian-free Newton–Krylov method. This method relies on an iterative solver and the computation of the residual, while the Jacobian (or an approximation to the Jacobian) is used for preconditioning. The Jacobian is calculated by differentiating the equation with respect to the primary variable. Eqs. 38–40 give the Jacobian corresponding to Eqs. 35–37 respectively.

$$\left(\frac{\psi_j}{\Delta_t},\psi_i\right) + \left(D\nabla\psi_j + \frac{D\psi_j Q^*}{RT^2}\nabla T,\nabla\psi_i\right) + (\alpha^2\psi_j,\psi_i) = 0 \tag{38}$$

$$\left(\frac{\psi_j}{\Delta_t},\psi_i\right) + \left(D\nabla\psi_j + \frac{D\psi_j Q^*}{RT^2}\nabla T,\nabla\psi_i\right) + (\beta^2\psi_j,\psi_i) = 0 \tag{39}$$

$$\left(\frac{\psi_j}{\Delta_t},\psi_i\right) + \left(D\nabla\psi_j + \frac{D\psi_j Q^*}{RT^2}\nabla T,\nabla\psi_i\right) = 0 \tag{40}$$

Both the weak form and the Jacobian of the equations governing the concentration of hydrogen in solid solution have been implemented in BISON in order to perform hydrogen distribution calculations.

### 3.2. Implementation of the equation governing the hydrogen in the hydrides

The equation governing the balance of hydrogen in the precipitated hydride ($C_{pp}$) involves the time derivative of $C_{pp}$ and the concentration of hydrogen in solid solution ($C_{ss}$):

$$\frac{dC_{pp}}{dt} = f(C_{ss}) \tag{41}$$

This equation indicates that $C_{pp}$ does not have to be solved as a primary variable. Once the $C_{ss}$ solution is known, the calculation of $C_{pp}$ is straightforward through a simple updating scheme. Also, if $C_{pp}$ is calculated based on $C_{ss}$, no Jacobian is required. BISON supports the use of secondary variables in this manner.

For the precipitation case (case 1), Eq. (10) becomes:

$$\text{If}\quad C_{ss} > \mathrm{TSS}_p, C_{pp}(t_{n+1}) = C_{pp}(t_n) + \Delta_t\cdot\alpha^2\cdot(C_{ss} - \mathrm{TSS}_p) \tag{42}$$

In the hysteresis range (case 2), Eq. (11) becomes:

$$\text{If}\quad \mathrm{TSS}_p \geqslant C_{ss} > \mathrm{TSS}_d, C_{pp}(t_{n+1}) = C_{pp}(t_n) \tag{43}$$

For dissolution (case 3), Eq. (12) becomes:

$$\text{if}\quad \mathrm{TSS}_d \leqslant C_{ss}\ \text{ and }\ C_{pp} > 0\ \text{ and }\ \nabla J > 0,\quad C_{pp}(t_{n+1}) = C_{pp}(t_n) - \Delta_t\cdot\beta^2\cdot(\mathrm{TSS}_d - C_{ss}) \tag{44}$$

When there is only diffusion (case 4), Eq. (13) becomes:

$$\text{if}\quad \mathrm{TSS}_d \geqslant C_{ss}\ \text{ and }\ C_{pp} = 0, C_{pp}(t_{n+1}) = C_{pp}(t_n) \tag{45}$$

### 3.3. Implementation of the boundary condition

In order to solve the second-order partial differential equations that govern the concentration of hydrogen in solid solution, it is necessary to specify the boundary conditions. There are two ways to express these boundary conditions. The first one is to impose a given concentration at a boundary:

$$C_{ss}(x_0, y, z) = C_{BC} \tag{46}$$

The second one is to impose a flux at the boundary:

$$\boldsymbol{J} \cdot \boldsymbol{dS}(x_0) = J_0 \tag{47}$$

where bold indicates a vector quantity. It has to be noted that the hydrogen flux is given by Eq. (4) and is not directly proportional to the concentration gradient. Therefore, a zero-flux boundary condition does not imply that the solid solution concentration profile is flat. Indeed, if there is a temperature gradient, the concentration profile has to show a finite gradient in order to compensate for the flux induced by the Soret effect:

$$\boldsymbol{J} \cdot \boldsymbol{dS}(x_0) = 0 \tag{48}$$

$$\nabla C_{SS} \cdot \boldsymbol{dS} = -\frac{DC_{SS}Q^*}{RT^2} \nabla T \cdot \boldsymbol{dS} \tag{49}$$

As shown by Eq. (49) the concentration gradient $\nabla C_{ss}$ is not equal to 0 if the temperature gradient is not equal to 0. Therefore, in the hydrogen model, the Neumann boundary condition corresponds to the specific flux boundary condition and not to the derivative of the primary variable. A specific boundary condition has been created for the hydrogen flux at the interface of the coolant and the cladding. Since no oxide layer has been yet modeled in BISON, this flux is calculated from the MATPRO theoretical oxide growth, detailed in Section 2.4. BISON calculates the flux at integration points along the cladding/coolant interface and uses this value in the balance equation. In all the other boundary locations, the hydrogen flux is assumed to be equal to 0.

## 4. Test cases of the hydrogen model

### 4.1. Geometry and materials

The model is tested under various simple conditions. The simulations are performed on Zircaloy-4 using the constants given in Table 2.1. A plate geometry of 660 μm (typical thickness for a PWR Zircaloy-4 cladding) is used. This simple 1-dimensional geometry allows a straightforward interpretation of the calculated solutions. However, it does not accurately reproduce all the particularities of the fuel cladding geometry, in particular the axial transport of hydrogen and specific geometrical features such as the inter pellet gap or the effect of the spacer grids. In the simulations performed on this mesh, the temperature varies only radially and there are 22 nodes in the radial direction.

### 4.2. Case 1: hydrogen distribution under a temperature gradient before precipitation

This simulation reproduces the first step in hydrogen redistribution. A constant temperature gradient of 60.6 °C/mm in the r direction has been assumed, corresponding to a temperature going from 320 °C at the coolant/cladding interface to 360 °C at the fuel/cladding interface. Since there is no heat source in the cladding and the conductivity is nearly constant with temperature, the temperature gradient is linear. The hydrogen flux due to oxidation is given by Eq. (29).

At each time step, the distribution of hydrogen is close to the equilibrium level, given by Eq. (6). Fig. 4.1 shows the evolution of the profile for 1 year. After 1 year, the average hydrogen concentration is low (about 8 wt. ppm). Hydrogen redistributes in the cladding in response to the temperature gradient. According to the Soret effect; this leads to an accumulation of hydrogen on the colder side of the cladding ($r = 0$ μm in Fig. 4.1). The difference between the highest and the lowest concentration increases as the average concentration increases. Thus, the Soret effect is more visible after 1 year than at the beginning of the simulation.

Since the $TSS_p$ decreases with temperature, the lowest $TSS_p$ is observed at the outer edge of the cladding. According to the results above, this is also where the concentration of hydrogen in solid solution is at its highest (with respect to the radial profile). So this is where precipitation is expected first. However, as long as this concentration is below the $TSS_p$ at 320 °C, there is no precipitation and the equilibrium solution given by Eq. (6) is observed.

### 4.3. Case 2: simulation of the consequences of a reactor shutdown

Most of the hydrogen measurement and cross-sectional pictures performed in the literature are post-facto measurements [4,5,37]. Therefore, what is observed is not the actual hydrogen distribution during reactor operation at temperature but rather the hydride distribution at low temperature after a normal reactor shutdown. This case aims to study the changes brought to the hydride distribution upon shutdown.

#### 4.3.1. Reactor shutdown parameters

Reactor shutdown takes place in two phases. First, the control rods are moved down in order to stop the chain reaction, causing the reactor to go from Hot Full Power (HFP) to Hot Zero Power (HZP), an operation that takes about two minutes. Once the control rods are down, only the heat produced by the radioactive decay of the fission products remains. At this point, the temperature in the core is almost homogeneous due to the relatively low power (less than 7% full power) and correspondingly low heat flux. Then the main and auxiliary cooling systems are used to bring temperature and pressure to room and atmospheric conditions. Usually, the temperature is decreased linearly within 24 h, as explained in the NRC Standard Technical Specifications [38]. In the current simulation, the coolant temperature is decreased linearly from 320 °C to 20 °C.

The decay heat is calculated as a percentage of the nominal power by the American Nuclear Society standard, as described in [39]. The power from decay heat as a function of time (starting at HZP) is given by:

$$P(t, \infty) = P_0 \cdot A \cdot t^{-a} \tag{50}$$

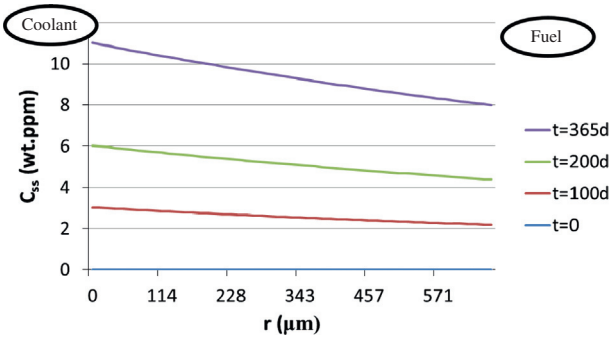


**Fig. 4.1.** Hydrogen in solid solution during 1 year exposure under a typical cladding radial temperature gradient (60 °C/mm).

The infinity sign means the equation approximates an infinite time of operation before the shutdown. $P_0$ is the nominal power produced by the fuel at the start of each interval shown in Table 4.1. For each interval, A and a are constants given in Table 4.1.

If the heat rate and the outer cladding temperature are known, the inner cladding temperature can be calculated using the equation:

$$T_{\text{inner}} = T_{\text{outer}} + \frac{q'_{\text{nominal}}}{k_{\text{cladding}}} \cdot \frac{P}{P_0} \cdot \frac{th_{Zr}}{2\pi(R_{\text{inner}} + l/2)} \quad (51)$$

with $q'_{\text{nominal}}$ the nominal linear heat rate just prior to shutdown, $k_{\text{cladding}}$ the conductivity of the cladding, $P/P_0$ the factor given by Eq. (50), $R_{\text{inner}}$ the inner cladding radius, $th_{Zr}$ the oxide thickness.

Assuming a linear heat rate of 18.5 kJ/m, the inner cladding temperature is very close to that of the outer cladding. Right after shutdown, the temperature difference is about 1.5 °C. After 1 h, the difference is less than 0.5 °C. At the end of 1 day, the difference is smaller than 0.2 °C. As a consequence, the temperature is almost constant in the cladding after the Hot Zero Power condition is achieved. The small temperature gradient and the low temperature indicates that it is unlikely there could be significant hydrogen redistribution during shutdown, although much of the hydrogen in solid solution may redistribute.

### 4.3.2. Simulation of the hydrogen redistribution during shutdown

The simulation considers a shutdown occurring at a time when the average hydrogen content in the cladding is 120 wt. ppm, homogeneously distributed. The simulation was run for 2.31 days using the temperature deduced from the constant heat flux and the cladding temperature (linear gradient between 330 and 360 °C). This leads to the formation of a small hydride rim. The shutdown starts at 2.31 days and takes 24 h. After the shutdown, temperature is held at 20 °C held for 3 more days, in order to verify that there is no further hydrogen evolution at room temperature.

The temperature and concentration were followed in 7 nodes, from the outer cladding to the inner cladding, numbered from 1 to 7. Fig. 4.2 shows the evolution of temperature with respect to time for these nodes. The temperature profiles are consistent with the conditions detailed in Section 4.3.1. The temperature gradient disappears when the shutdown begins, since the difference in temperature due to decay heat is too small to be seen on the graphs. Following shutdown, the temperature decreases linearly to room temperature in 24 h. Fig. 4.3 shows the evolution of the hydrogen in solid solution. The $C_{ss}$ profile is quickly homogenized when the conditions go from HFP to HZP, because without a temperature gradient, the Soret effect disappears. Only Fick's law remains, which tends to homogenize the $C_{ss}$ concentration in the cladding. Following the homogenization, the cladding is cooled down and the $TSS_p$ progressively decreases. As hydrogen precipitates, the hydrogen concentration in solid solution decreases. As the temperature decreases, the precipitation kinetics slows down, so that not all the hydrogen is precipitated at the end of the simulation. The concentration of hydrogen in the hydrides is shown in Fig. 4.4. As mentioned above, before shutdown, a hydride rim is formed in the first 2 nodes, close to the outer edge of the cladding, as expected. Because the simulation ran for only 3 days, the concentration of hydrogen in hydrides is lower than 350 wt. ppm. Once the shutdown occurs, hydrides appear throughout the cladding, as a result of precipitation of the hydrogen from solid solution.

**Table 4.1**
Shutdown decay power constants.

| Time interval (s) | A | a |
|---|---|---|
| $0.1 < t < 10$ | 0.0603 | 0.0639 |
| $10 < t < 150$ | 0.0766 | 0.181 |
| $150 < t < 4 \times 10^6$ | 0.130 | 0.283 |
| $4 \times 10^6 < t < 2 \times 10^8$ | 0.266 | 0.335 |

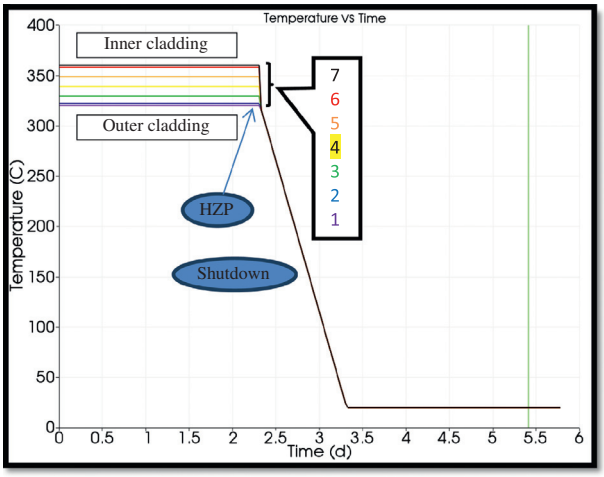


**Fig. 4.2.** Temperature vs. time for case 3.

The results show that the shutdown has little effect on the hydrides formed during reactor operation. As mentioned above, the small gradient also means little hydrogen transport. However, hydrogen that was in solid solution during operation redistributes and precipitates homogeneously. This potentially explains why some hydrides are also seen in the metal substrate underneath the rim, in cross sectional micrographs taken of samples with a hydride rim, as shown in Fig. 4.5.

## 4.4. Case 3: hydride rim formation

In a second calculation, the formation of a hydride rim is studied. The BISON simulation time was 1 year. The initial concentration is assumed to be equal to 127 wt. ppm homogeneously distributed. The linear temperature gradient is 45.5 °C/mm. The $TSS_p$ at 330° is equal to 143 wt. ppm according to Eq. (5) (i.e. just above the concentration seen at the colder spot due to the Soret effect). For this simulation, 52 radial nodes were used to obtain an accurate prediction of the hydrogen concentration.

As the simulation starts, the $TSS_p$ concentration is reached almost immediately in the outer wall area due to the Soret effect.

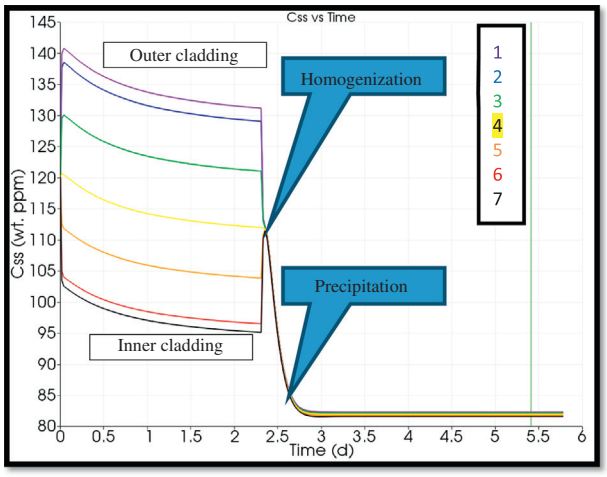


**Fig. 4.3.** Hydrogen in solid solution vs. time for case 3.

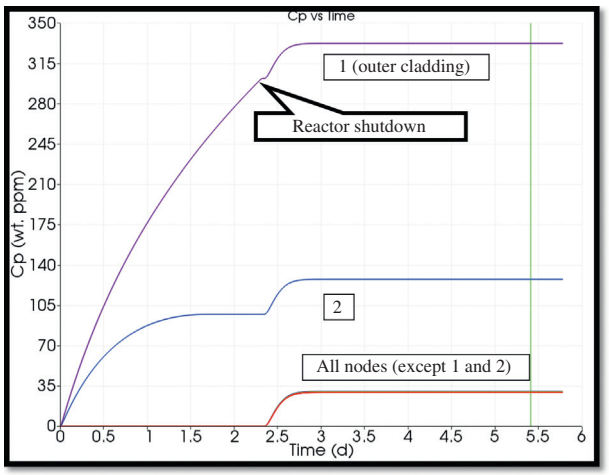


**Fig. 4.4.** Hydrogen in hydrides vs. time for case 3.

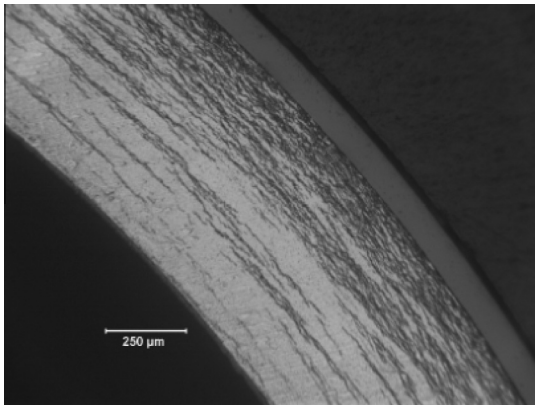


**Fig. 4.5.** Hydride distribution and morphology in HBR rod F07 cladding near 650 mm above midplane (740-wppm through thickness average hydrogen concentration) [4].

The temperature profile is kept constant for the run. For this run, the hydrogen flux has been artificially increased with a factor of 10 to allow speeding up the simulation to emphasize the hydrogen distribution features. Thus, although the diffusion simulation was run for 1 year, the pickup rate at the surface simulates 10 years of corrosion.

In order to understand the formation of the rim, it is necessary to observe the consequences of the balance equations. Due to the Soret effect, at the end of a given timestep, the concentration of hydrogen in the first node (near the outer wall) reaches the $TSS_p$. This causes a driving force for precipitation $\Delta C = C_{ss} - TSS_p$. During the next timestep, precipitation terms appear in the equation and the fraction $\alpha \cdot \Delta C \cdot \Delta_t$ precipitates. The remainder $(1 - \alpha) \cdot \Delta C \cdot \Delta_t$ stays in supersaturation in the node. This increases the inward diffusion flux toward the next node.

Examining the further behavior of the second node, two outcomes can occur, noting that the $TSS_p$ in the second node is higher than the $TSS_p$ in the first. If the hydrogen diffused from the first node is not sufficient to reach the new local $TSS_p$, a new solid solution profile is obtained which follows the standard equilibrium, expressed in Eq. (6). If on the other hand, the concentration in the 2nd node exceeds the new $TSS_p$, precipitation occurs. Again, a fraction of the hydrogen in solid solution precipitates while another fraction stays in solid solution.

Eventually in the first node, the hydrogen flux coming from the boundary will equal the sum of the hydrogen diffusing and the hydrogen precipitating. Once this equilibrium is reached, the concentration in solid solution becomes constant in the location where the hydrogen has precipitated. In addition to this mechanism, once the precipitated hydrogen $C_{pp}$ reaches the pre-defined 1000 wt. ppm rim limit, it diffuses toward the inner edge of the cladding.

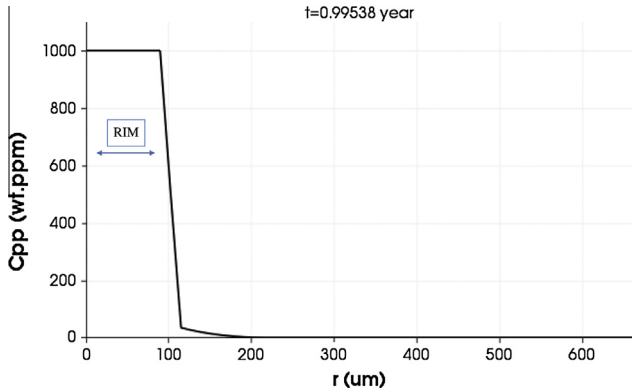


**Fig. 4.6.** Hydride profile after 1 year of precipitation with a limit of 1000 wt. ppm of hydrogen in hydrides.

Fig. 4.6 shows the distribution of precipitated hydrogen concentration ($C_{pp}$) after 1 year. A rim has developed whose thickness is about 80 μm. The growth of the rim is shown in Fig. 4.8 and is quasi linear. The rim increases with increasing simulation time or if the oxidation rate or the hydrogen pick up fraction are increased. Fig. 4.7 shows the concentration of hydrogen in solid solution after 1 year. The hydrogen concentration in solid solution is higher than what it would be without any precipitation because

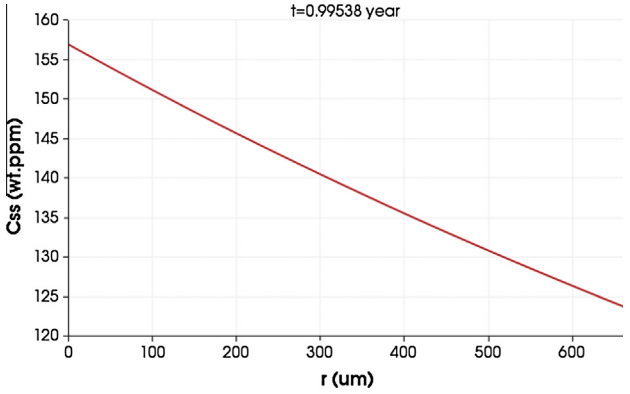


**Fig. 4.7.** Hydrogen in solid solution after 1 year of precipitation with a limit of 1000 wt. ppm of hydrogen in hydrides. The zero position is the outer cladding surface.

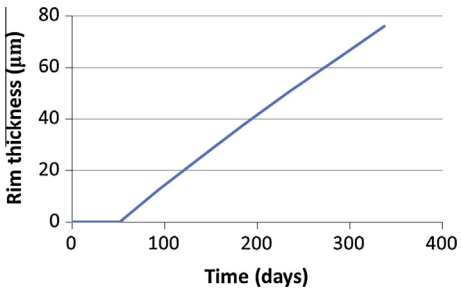


**Fig. 4.8.** Evolution of the rim thickness with time for 1 year. The hydrogen concentration at the start of the simulation is 127 wt. ppm.

the elements close to the coolant interface are filled with the maximum hydride concentration. Although the thickness of the rim would appear to be larger than what would be expected to be achievable with such low overall hydrogen concentrations, these results show the correct physical direction and phenomena.

## 5. Conclusions

This study documents the successful implementation of a hydrogen model for the fuel performance code BISON. Based on previous modeling of diffusion and precipitation laws, a model was established and implemented into BISON. This creates a tool capable of predicting the hydrogen and hydride distribution in any geometry. This tool is fully integrated in the code and is available to BISON users. Simulations performed on a simplified 1D geometry show consistent results with previous observations.

The first simulation predicts that hydrogen accumulates on the colder spots of the cladding, as expected, due to the Soret effect.

The second simulation shows that reactor shutdown has a limited effect on the hydride distribution. The main effect is that the hydrogen that was in solid solution is homogenized and then precipitated into hydrides during the shutdown. This explains the presence of hydride precipitates in the previously hot areas of the cladding on post-facto micrographs taken at room temperature.

The third simulation shows that the thickness of the hydride rim is highly dependent on the maximum value established for the amount of hydrides per unit of volume. The maximum total hydrogen concentrations in the rim are usually measured between 1000 and 2000 wt. ppm. By setting it at these values, the calculation predicts a reasonable thickness for the rim ($\sim$60 μm) that corresponds to experiments.

Future work in this project will include calculation of hydrogen distribution in more realistic geometries, such as occur in fuel rods. This will allow the evaluation of the azimuthal and axial hydrogen distributions. A limitation to the model is that no oxide layer is modeled by BISON yet. This affects the calculation of the temperature at the coolant/cladding interface, where the oxide is usually formed. An improvement of BISON performance in this area would result in a corresponding improvement of the calculation of the hydrogen redistribution.

## Acknowledgements

This research was funded by DOE NEUP project 11-2987 of the US Department of Energy. This work is the result of collaborative project between Penn State University and the Idaho National Laboratory, which also includes Maria Avramova (PSU), Ian Davis (PSU), Kostadin Ivanov (PSU) and Richard Williamson (INL). We would like to thank Matthew Lindenberg for his help in configuring BISON. We would also like to thank Kevin Cass for his assistance in the analysis of the results during his Toshiba-Westinghouse Undergraduate Fellows program internship at Penn State.

The submitted manuscript has been authored by a contractor of the US Government under Contract DE-AC07-05ID14517. Accordingly, the US Government retains a non-exclusive, royalty free license to publish or reproduce the published form of this contribution, or allow others to do so, for US Government purposes.

## References

[1] S. Yamanaka, K. Yoshioka, M. Uno, M. Katsura, H. Anada, T. Matsuda, S. Kobayashi, J. Alloy. Compd. 293–295 (1999) 23–29.
[2] A. Racine, Influence de l'orientation des hydrures sur les modes de deformation, d'endommagement et de rupture du Zircaloy-4 hydrure, PhD thesis, Mecanique et Materiaux, L'Ecole Polytechnique, 2005.
[3] R.S. Daum, S. Majumdar, H.C. Tsai, M.C. Billone, D.W. Bates, D.A. Koss, A.T. Motta, Embrittlement of Hydrided Zircaloy-4 under RIA-like conditions, in: 13th ASTM International Symposium on Zr in the Nuclear Industry, Annecy, France, 2001, ASTM STP 1423, pp. 702–719.
[4] M. Billone, Y. Yan, T. Burtseva, R. Daum, NRC (2008).
[5] P. Bossis, D. Pecheur, K. Hanifi, J. Thomazet, M. Blat, J. ASTM Int. 3 (2006). p. paper IDJAI12404.
[6] G. Zhou, J. Arborelius, L. Hallstadius, M. Limback, J. Nilsson, K. Backman, B. Rebensdorff, G. Hede, K. Kitano, G. Ronnberg, Westinghouse advanced $UO_2$ fuel behaviors during power transients, in: 2005 Water Reactor Fuel Performance Meeting, Kyoto, Japan, 2005, pp. 147–156.
[7] A. Garde, S.R. Pati, M.A. Krammen, G.P. Smith, R.K. Endter, in: Zirconium in the Nuclear Industry: Tenth International Symposium, Baltimore, MD, USA, 1994, ASTM STP 1423, pp. 760–778.
[8] A. Hermann, S.K. Yagnik, D. Gavillet, Effect of local hydride accumulations on zircaloy cladding mechanical properties, Sunriver, OR, United States, 2009, ASTM STP 1505, pp. 141–162.
[9] M.P. Puls, B.W. Litch, S.-Q. Shi, The effect of applied stress on the accommodation energy and the solvi for the formation and dissolution of zirconium hydride, in: International Conference on Hydrogen Effects on Material Behaviour and Corrosion Deformation Interactions, Sep 22–26 2002, Moran, WY, United States, 2003, pp. 233–248. (BN-0873395018).
[10] B.F. Kammenzind, B.M. Berquist, R. Bajaj, P.H. Kreyns, D.G. Franklin, The long-range migration of hydrogen through Zircaloy in response to tensile and compressive stress gradients, in: Zirconium in the Nuclear Industry: Twelfth International Symposium, ASTM STP 1354, 2000, pp. 196–233.
[11] J.J. Kearns, J. Nucl. Mater. 43 (1972) 330–338.
[12] A. Sawatzky, J. Nucl. Mater. 2 (1960) 62–68.
[13] A. Sawatzky, J. Nucl. Mater. 9 (1963) 364.
[14] M. Sugisaki, K. Hashizume, Y. Hatano, Estimation of hydrogen redistribution in zircaloy cladding of spent fuel under thermal conditions of dry storage and evaluation of its influence on mechanical properties of the cladding, IAEA-TECDOC-1316, Vienna, Austria, 2002.
[15] S. Morozumi, M. Kitada, K. Abe, S. Koda, J. Nucl. Mater. 33 (1969) 261–270.
[16] K. Hashizume, M. Hayakawa, M. Koganemaru, M. Sugisaki, Defect Diffusion Forum 95–98 (1993) 323–328.
[17] J. Markowitz, Trans. Metall. Soc. AIME 221 (1961).
[18] W. Kiauka, C.v. Cuyck, W. Keune, Mater. Sci. Eng. B12 (1992) 273–279.
[19] Y. Choi, J.W. Lee, Y.W. Lee, S.I. Hong, J. Nucl. Mater. 256 (1998) 124–130.
[20] M. Jovanovic, A. Stern, G. Kneis, G. Weatherly, M. Leger, Can. Metall. Q. 1 (1) (1988) 323–330.
[21] B.F. Kammenzind, D.G. Franklin, H.R. Peters, W.J. Duffin, in: 11th International Symp on Zr in the Nuclear Industry, 1996, ASTM STP 1245, pp. 338–370.
[22] D. Kondepudi, I. Prigogine, Modern Thermodynamics, John Wiley & Sons, 1998.
[23] A. Sawatzky, J. Nucl. Mater. 2 (1960) 321–328.
[24] J.J. Kearns, Terminal solubility and partitioning of hydrogen in the alpha phase of zirconium, Zircaloy-2 and Zircaloy-4, J. Nucl. Mater. 22 (1967) 292–303. 1967/6.
[25] A. McMinn, E.C. Darby, J.S. Schofield, The terminal solid solubility of hydrogen in zirconium alloys, in: 12th Int. Symp. on Zr in the Nuclear Industry, Toronto, CA, 2000, ASTM STP 1354, pp. 173–195.
[26] P. Shewmon, Trans. Metall. Soc. AIME 212 (1958) 642–647.
[27] G.P. Marino, Mater. Sci. Eng. 7 (1971) 335–341.
[28] G.P. Marino, HYDIZ: A 2-dimensonal computer program for migration of interstitial solutes of finite solubility in a thermal gradient (LWBR Development Program), WAPD-TM–1157, 1974.
[29] IAEA, Waterside Corrosion of Zirconium Alloys in Nuclear Power Plants, International Atomic Energy Agency, Vienna TECDOC996, 1998.
[30] F. Garzarolli, R. Manzel, S. Reschke, E. Tenckhoff, Review of corrosion and dimensional behavior of zircaloy under reactor water conditions, 1979, ASTM STP 681, p. 91.
[31] A. Yilmazbayhan, E. Breval, A. Motta, R. Comstock, J. Nucl. Mater. 349 (2006) 265–281.
[32] L.J. Siefken, E.W. Coryell, E.A. Harvego, J.K. Hohorst, MATPRO – A library of materials properties for light-water-reactor accident analysis, SCDAP/RELAP5/MOD 3.3 Code Manual, Vol. 4, Rev. 2, NUREG/CR–6150, 2001.
[33] C.E. Coleman, D. Hardie, J. Less-Common Met. 2 (1966) 168–185.
[34] A. Couet, A.T. Motta, R.J. Comstock, J. Nucl. Mater. 451 (2014) 1–13.
[35] R.L. Williamson, J.D. Hales, S.R. Novascone, M.R. Tonks, D.R. Gaston, C.J. Permann, D. Andrs, R.C. Martineau, J. Nucl. Mater. 423 (2012) 149–163.
[36] C. Newman, G. Hansen, D. Gaston, J. Nucl. Mater. 392 (2009) 6–15.
[37] IAEA, Review of fuel failures in water cooled reactors, Doc.No # NF-T-2-1, 2010.
[38] U.S.NRC, Standard Technical Specifications –Westinghouse plants, ed: Office of Nuclear Reactor Regulation, NRC, NUREG–1431, 2012.
[39] R. Cochran, N. Tsoulfanidis, The Nuclear Fuel Cycle, American Nuclear Society, 1999.